A phase-field method for three-phase flows with icing

Wenqiang Zhang[a], Armin Shahmardi[b], Kwing-so Choi[a], Outi Tammisola[b], Luca Brandt[b], Xuerui Mao[a]

Corresponding author: Xuerui Mao, maoxuerui@sina.com

[a]University of Nottingham, University Park Campus, Nottingham NG7 2RD, UK

[b]SeRC (Swedish e-Sience Research Centre) and Flow, KTH, Department of Engineering Mechanics, SE-10044 Stockholm, Sweden.

Abstract

A numerical scheme to simulate three-phase fluid flows with phase change is proposed. By combining the Cahn-Hilliard model for water-air interface, Allen-Cahn equation for ice and fluid and Navier-Stokes equation for momentum, we solve the evolution of the water-air interface and water-ice interface simultaneously, including the volume expansion associated with solidification and due to the density difference between water and ice. Unlike existing schemes assuming a divergence-free flow field, the proposed continuous formulation allows for density changes while ensuring mass conservation. A Poisson equation for the pressure field is derived from mass conservation with constant coefficients, which can efficiently be solved without any pre-conditioning. The results demonstrate that the volume expansion during the ice formation and the subsequent motion of the water-air interface are successfully captured. A parametric study is carried out to examine the dependence of the icing on different physical and numerical parameters. Computations with flow disturbance of different amplitudes demonstrate the robustness of the computational scheme and the uniqueness of the solution over the parameters considered.

1. Introduction

The phase-field method [1, 2] has been widely used for the multiphase flow simulations. Compared with the volume-of-fluid method [3, 4], the level-set method [5, 6] and the front-tracking method [7, 8], the main advantage of the phase-field method is that the interface can be resolved without introducing dedicated boundary conditions. In addition, the approach is thermodynamically motivated and the system is characterized by a free energy which allows different physical effects to be accounted for by suitable modifications of the free energy. By combining with the Navier-Stokes (NS) equations to model the convection of the interface, the phase-field method has been successfully used to model the contact-line motion problem [9, 10] and other immiscible two-phase flows without phase change [11, 12, 13]. In these simulations, the flow field is considered as incompressible, i.e., $\triangledown \cdot \vec{U} = 0$, where $\vec{U}$ denotes the velocity vector. The phase-field method is also widely used in the simulations of phase change such as solidification [14, 15], melting [16], boiling [17] and sublimation [18]. Among others, phase-field models for the solidification of a pure material including convection in the liquid phase was developed in [19, 20].Except for most of the alloys [21, 22], the phase change between solid and liquid might be accompanied by significant volume expansion or contraction, examples being water [23, 24] and silicon in which case the two phases have a non-negligible density difference. This leads to a flow away from or towards the liquid-solid interface when solidification or melting occurs. Therefore, both the density change and the induced convection of the flow must be incorporated in the computations to avoid unphysical results. It can be shown that in the case of solidification with density difference [25, 26], the velocity field is not solenoidal (divergence-free) and thus $\triangledown \cdot \vec{U} \neq 0$. In the computational model in [26], each phase possesses different velocity at the interface and the velocity of the mixture is a mass-averaged value of all the species. This will result in a higher computational cost as the number of phases increases.

Besides the above-mentioned work on two-phase flows, phase-field models for incompressible, three-component immiscible fluid flows without phase change have also been developed, see e.g. [28, 29, 30]. The existence of gas surrounding the liquid can influence the solidification of a liquid. For example, it was shown experimentally

that the shear from the gas flow around the water droplet can affect its freezing on a solid surface in terms of icing speed, location and direction of the freezing front, and hence the final shape of the ice [31]. Therefore, the accurate simulation of the solidification of a liquid requires taking the ambient gas flow into consideration. There has been a limited number of numerical studies of solidification phenomena in three-phase flows using the phase-field method, i.e., considering the evolution of the liquid-solid interface and liquid-gas interface simultaneously. Such a simulation needs to accurately solve a liquid-solid density difference and possible large liquid-gas density ratio. The interface evolution, flow convection, and the heat transfer within and between different phases need to be accurately modelled. To the best of the authors' knowledge, only one previous study has applied the phase-field method to three-phase icing simulations [32]. However, in that work the convection in the solidification process is ignored, the density difference between the water and the ice resulting in an expansion of the ice is not considered and instead the ice-water interface is treated with an immersed boundary method.

In addition to the physical modelling, another issue with the phase-field method is the numerical scheme to solve the incompressible NS equation to obtain the pressure and velocity of the multiphase flow field. A routinely used numerical scheme is the projection method in which a Poisson equation is constructed and solved to obtain the pressure of the flow field at every time step. For the two-phase flow with a large density ratio, a typical temporal discretization of the Poisson equation is as follows:

$$\nabla \cdot (\frac{1}{\rho^{n+1}} \nabla P^{n+1}) = \frac{1}{\Delta t} \nabla \cdot \vec{U}^*,$$ (1)

where ρ^{n+1} is the density and P^{n+1} is the pressure at time step $n + 1$; Δt is the time step in the temporal discretization and $\vec{U}^*$ is the approximate velocity at time step $n + 1$. As the density ρ^{n+1} is a function of the phase-field parameter, the coefficient of the Poisson equation is time- and space- dependent which prohibits the use of some fast Possion solvers. As a result, pre-conditioning of the Poisson equation, such as the penalty formulation [33] or the velocity-correction method [34, 35] is needed especially for large density ratio problems. By adopting the continuous equation instead of the divergence-free condition, we can derive a Poisson equation with a constant coefficient without any pre-conditioning to solve the three-phase flows with phase change and large density ratio.

In this paper, we report a comprehensive numerical model and discretization scheme for the solidification in the presence of a liquid and an inert gas phase. The ice-water-air system with the icing process with the background application in aeronautics is adopted to demonstrate this approach. We consider that the strategy is general and can be applied to other three-phase systems. The outline of this paper is as follows: in Section 2, the phase-field model and the governing equation system are introduced. Section 3 describes the numerical scheme and the discretizations of the equation system. The one-dimensional test cases are presented in Section 4. In Section 5, we conduct a parametric study on the icing problem, varying mobility, wall temperature and interface thickness. In the last section, we summarise the properties of the proposed numerical scheme and the simulation results as well as the potential extensions of the present work.

2. Mathematical description

2.1. Phase-field modelling

The basic idea of this work is to use a phase-field approach introducing two order parameters that vary continuously over thin interface layers between liquid-solid and liquid-gas [8]. The aim is to study the solidification process of water in the ice-water-air ternary phase system. "Water", "ice" and "air" are used to denote the pure liquid, solid and gas phases, respectively. We assume that ice is only formed within water (water vapor in the air is not considered) and water and air are immiscible. In our simulation, the phase-field variable, ϕ, as a function of position and time, is employed to distinguish whether the medium is water-ice mixture (the liquid phase and solid phase coexist) or air. Here, $\phi = 1$ means a mixture of water and ice while $\phi = -1$ denotes pure air. The second phase-field variable, c, is used to describe the volume fraction of ice in the water-ice mixture:

$$c = -\frac{V_{ice}}{V_{ice} + V_{water}},$$ (2)

where V_{ice} and V_{water} denote the local volume within a very small neighbourhood. We set that $-1 \leqslant \phi \leqslant 1$ and $-1 \leqslant c \leqslant 0$. As shown in Fig. 1, $\phi = 1$ & $c = 0$ represents pure water, $\phi = 1$ & $c = -1$ represents pure ice and

$\phi = -1$ & $c = 0$ denotes pure air. The position of the water-air interface is $\phi = 0$ and $c = 0$ stands for water-ice interface. In the pure air phase, c is always 0. It is noted that phase change only occurs between water and ice.

air, ϕ=-1, c=0
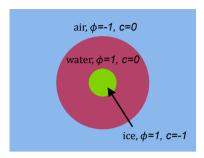
water, ϕ=1, c=0

ice, ϕ=1, c=-1

Fig. 1: A sketch of the three phases distinguished by phase-field order parameters.

The material properties (density, viscosity and thermal conductivity coefficient) of each single phase are fixed. In this paper, the solid phase (ice) and the liquid phase (water) are represented as Newtonian fluids. The viscosity of the solid phase is specified to be far larger than that of the liquid phase [19] to reduce its movement. Denoting air, water and ice as phase 1, phase 2 and phase 3, the material properties of the mixture are defined as linear functions of the phase-field order parameters through the constitutive equations:

$$\rho(\phi, c) = \frac{1}{2}(\phi + 1) \cdot [(c + 1)\rho_2 - c\rho_3] - \frac{1}{2}(\phi - 1)\rho_1, \tag{3}$$

$$\eta(\phi, c) = \frac{1}{2}(\phi + 1) \cdot [(c + 1)\eta_2 - c\eta_3] - \frac{1}{2}(\phi - 1)\eta_1, \tag{4}$$

$$k(\phi, c) = \frac{1}{2}(\phi + 1) \cdot [(c + 1)k_2 - ck_3] - \frac{1}{2}(\phi - 1)k_1, \tag{5}$$

where η is the viscosity and k is the thermal conductivity of the mixture.

2.2. Governing equations

The Cahn-Hilliard (CH) equation is used to model the evolution of the interface between water and air:

$$\frac{\partial \phi}{\partial t} + \triangledown \cdot (\phi \vec{U}) = M_\phi \triangledown^2 \mu_\phi - \phi \triangledown \cdot \vec{U}. \tag{6}$$

Here we start from the thermodynamically consistent model introduced in [53]. $\vec{U}$ is the volume averaged velocity of the mixture, since there is no need to distinguish the velocity of each single component as adopted in [26]. As volume expansion exists during the icing process, the source term $-\phi \triangledown \cdot \vec{U}$ cannot be ignored. The phenomenological mobility M_ϕ is computed as $M_\phi = 2\sqrt{2}u_{ref}\xi_\phi l_{ref}/(3\sigma_\phi \cdot Pec)$, where u_{ref} is the reference velocity, σ_ϕ is the surface tension coefficient, ξ_ϕ is the thickness of the interface between water and air, and l_{ref} is the reference length. We choose the mobility to be independent of ϕ. Pec is the Peclet number which expresses the ratio between advection and diffusion. μ_ϕ is the chemical potential for the water-air system:

$$\mu_\phi = -\frac{3}{2\sqrt{2}}\sigma_\phi \xi_\phi \triangledown^2 \phi - \frac{3\sigma_\phi}{2\sqrt{2}\xi_\phi}(\phi - \phi^3). \tag{7}$$

It is noted that while the conservative form term is used in Eq. (6), an additional term $\phi \triangledown \cdot \vec{U}$ is added to the RHS of the equation as a source term. Eq. (6) cannot be simplified as:

$$\frac{\partial \phi}{\partial t} + \vec{U} \cdot \triangledown \phi = M_\phi \triangledown^2 \mu_\phi. \tag{8}$$

Considering that the liquid and gas are basically incompressible ($\triangledown \cdot \vec{U} = 0$), we have $\triangledown \cdot (\vec{U}\phi) = \vec{U} \cdot \triangledown \phi + \phi \triangledown \cdot \vec{U} = \vec{U} \cdot \triangledown \phi$ at the water-air interface. However, Eq. (11) implies that the divergence of the velocity is not necessarily zero. This occurs at the liquid-solid interface when the solidification evolves with density difference.

The Allen-Cahn (AC) equation is used to simulate the phase change from water to ice [36] :

$$\frac{\partial c}{\partial t} + \triangledown \cdot (\vec{\mathbf{U}} c) = M_c [6\sigma_c \xi_c \triangledown^2 c - \frac{\partial f_c}{\partial c}]. \tag{9}$$

In the AC equation, the mobility M_c is calculated as $M_c = 6\xi_c L [1/\omega + 5\xi_c L/6k]/T_M$, where ω is a parameter related to velocity and temperature at the water-ice interface; by adjusting the value of ω, the mobility of the icing process can be modified. L is the latent heat of fusion and T_M is the melting point of ice, while ξ_c is the thickness of the water-ice interface. On the right hand side of the AC equation, f_c is the free energy density given by [36]:

$$f_c = 3 \frac{\sigma_c}{\xi_c} g(c) + L \frac{T_M - T}{T_M} h(c). \tag{10}$$

It contains two terms: a double well function $g(c)$ and an interpolating function $h(c)$. The double well function describes the free energy density of the bulk of each phase and the interpolating function combines the free energies of liquid and solid. Here we choose the two functions, $g(c) = (c+1)^2 c^2$ and $h'(c) = 30g(c)$, respectively [36]. T is the temperature of the flow field.

The water-ice interface is assumed isotropic in this study, but any anisotropic model can be directly adopted. The computation of the AC equation is only carried out in water where $\phi > -1$ while the CH equation is solved in all three phases.

The continuity equation guarantees the total mass conservation during the simulation:

$$\frac{\partial \rho}{\partial t} + \triangledown \cdot (\rho \vec{\mathbf{U}} + \widetilde{J}) = 0, \tag{11}$$

where ρ is computed with Eq. (3) and $\widetilde{J} = -\frac{\rho_1 - \rho_2}{2} M_\phi \triangledown \mu_\phi$[53].

The thermodynamically consistent momentum equation is

$$\frac{\partial (\rho \vec{\mathbf{U}})}{\partial t} + \triangledown \cdot [(\rho \vec{\mathbf{U}} + \widetilde{J}) \otimes \vec{\mathbf{U}}] = - \triangledown P \cdot \overline{\overline{I}} + \triangledown \cdot \overline{\overline{\tau}} + \vec{F_b} + \text{SF}_{water-air} + \text{SF}_{water-ice}, \tag{12}$$

I is the unit diagonal tensor, $\vec{F_b}$ is body force (e.g., the acceleration of gravity) and $\overline{\overline{\tau}}$ is the stress tensor defined as $\overline{\overline{\tau}} = -2/3\eta \triangledown \cdot \vec{\mathbf{U}} \overline{\overline{I}} + \eta [\triangledown \vec{\mathbf{U}} + (\triangledown \vec{\mathbf{U}})^T]$, where $(\cdot)^T$ is the transpose of a matrix. The surface tension is $\text{SF}_{water-air} = \mu_\phi \triangledown \phi$ at the water-air interface and $\text{SF}_{water-ice} = \xi_c \triangledown c$ at the water-ice interface.

The temperature of the flow field is computed using the energy equation. The total energy of the control volume includes the kinetic energy and the free energy. The change of total energy in time is due to the work of surface forces, heat diffusion and phase change. The change of the free energy due to the movement of the water-ice interface is the latent heat. The effect of the movement of the water-air interface on the temperature change can be ignored in this study. The energy equation is as follows:

$$\frac{\partial (\rho C_p T)}{\partial t} + \triangledown \cdot (\rho C_p T \vec{\mathbf{U}}) = \frac{\partial V_3}{\partial t} \rho_3 L + \triangledown \cdot (k \triangledown T) + \Phi + \vec{\mathbf{U}} \cdot \vec{F_b}, \tag{13}$$

where V_3 is the volume fraction of ice in the mixture, $\frac{\partial V_3}{\partial t} \rho_3 L$ is the latent heat released during the icing process and Φ is the viscous dissipation $\Phi = (-2/3\eta \triangledown \cdot \vec{\mathbf{U}} \overline{\overline{I}} + \eta [\triangledown \vec{\mathbf{U}} + (\triangledown \vec{\mathbf{U}})^T]) : \triangledown \vec{U}$. η and k are computed with Eq. (4).

In summary, the governing equations for the aforementioned three-phase fluid flows with phase change are composed of mass conservation (11), momentum equations (12), the Cahn-Hilliard equation (6), the Allen-Cahn equation 9 and an energy equation (13). This leads to a closed system with 7 equations and 7 variables ($\vec{\mathbf{U}}$, ϕ, c, P and T) for three-dimensional simulations.

It is worth mentioning that there are various models to calculate the surface tension and chemical potentials in CH and AC equations [30]. As the main target of this work is to build a general numerical frame to model three-phase flows with phase change and the corresponding algorithm, only the common models are considered in the description below.

4

2.3. Procedure of the computation

Here, we first present the algorithm and then proceed to explain the different steps of it, focusing in particular on the novelty of the method. Throughout the paper, all flow field variables (density, velocity, pressure and temperature) are dimensional. The numerical algorithm to compute the solution of the governing equations at time step $n + 1$ is summarized as follows:

1. Calculate the value of ϕ and c of time step $n + 1$ with Eq. (6) and Eq. (9)
2. Obtain the density, thermal conductivity coefficient and viscosity at time step $n + 1$ using Eq. (3)-(5)
3. Advance the momentum equations to obtain the approximate velocity $\vec{\mathbf{U}}^*$ at time step $n + 1$
4. Compute P^{n+1} by solving the Poisson equation introduced below
5. Compute U^{n+1} using P^{n+1} and $\vec{\mathbf{U}}^*$
6. Calculate T^{n+1} using the second-order Crank-Nicolson scheme for the energy equation
7. Correct the velocity of ice and proceed to the next time step

In the first step, ϕ and c are computed explicitly. The density, viscosity and thermal conductivity obtained in the second step are used in the following calculations.

2.3.1. Projection method and the Poisson equation in Step 4

In this section, we derive a Poisson equation to compute the pressure imposing mass conservation. We start with the discretized form of the continuity equation at time step $n + 1$:

$$(\frac{\partial \rho}{\partial t})^{n+1} + \rho^{n+1} \triangledown \cdot \vec{\mathbf{U}}^{n+1} + (\vec{\mathbf{U}}^{n+1} \cdot \triangledown)\rho^{n+1} + \triangledown \cdot \widetilde{J}^{n+1} = 0. \tag{14}$$

We define RU^n as:

$$RU^n = -\triangledown \cdot [(\rho^{n+1}\vec{\mathbf{U}}^n + \widetilde{J}^{n+1}) \otimes \vec{\mathbf{U}}^n] + \triangledown \cdot \overline{\overline{\tau}}^n + \vec{F_b}^n + SF^n_{water-air} + SF^n_{water-ice}, \tag{15}$$

which is the right hand side of Eq. (12) without the pressure gradient. The calculation of $\overline{\overline{\tau}}^n$ and surface tension relies on $\vec{\mathbf{U}}^n$, ρ^{n+1} and η^{n+1} which are already available.

Eq. (12) is split into two equations:

$$\frac{\rho^{n+1}\vec{\mathbf{U}}^* - \rho^n\vec{\mathbf{U}}^n}{\Delta t} = RU^n \tag{16}$$

and

$$\frac{\vec{\mathbf{U}}^{n+1} - \vec{\mathbf{U}}^*}{\Delta t} = -\frac{1}{\rho^{n+1}} \triangledown P^{n+1}. \tag{17}$$

Rearranging Eq. (17) gives:

$$\vec{\mathbf{U}}^{n+1} = \vec{\mathbf{U}}^* - \frac{\Delta t}{\rho^{n+1}} \triangledown P^{n+1}. \tag{18}$$

Classically, the approximate velocity $\vec{\mathbf{U}}^*$ is computed with Eq. (16) and the velocity field at time step $n + 1$ is advanced with the correction of the pressure in Eq. (17). This is obtained by taking the divergence of Eq. (18)

$$\triangledown \cdot \vec{\mathbf{U}}^{n+1} = \triangledown \cdot \vec{\mathbf{U}}^* - \Delta t \triangledown \cdot (\frac{1}{\rho^{n+1}} \triangledown P^{n+1}) \tag{19}$$

and substituting $\triangledown \cdot \vec{\mathbf{U}}^{n+1}$ and $\vec{\mathbf{U}}^{n+1}$ in Eq. (14) with Eq. (19) and Eq. (18):

$$(\frac{\partial \rho}{\partial t})^{n+1} + \rho^{n+1}(\triangledown \cdot \mathbf{U}^* + \frac{\Delta t}{(\rho^{n+1})^2} \triangledown \rho^{n+1} \cdot \triangledown P^{n+1} - \frac{\Delta t}{\rho^{n+1}} \triangledown^2 P) + (\mathbf{U}^* - \frac{\Delta t}{\rho^{n+1}} \triangledown P^{n+1}) \cdot \triangledown \rho^{n+1} + \triangledown \cdot \widetilde{J}^{n+1} = 0. \tag{20}$$

Rearrange this equation yields the Poisson equation:

$$\triangledown^2 P^{n+1} = \frac{(\frac{\partial \rho}{\partial t})^{n+1} + \vec{\mathbf{U}}^* \cdot \triangledown \rho^{n+1} + \rho^{n+1} \triangledown \cdot \vec{\mathbf{U}}^* + \triangledown \cdot \widetilde{J}^{n+1}}{\Delta t} = \frac{(\frac{\partial \rho}{\partial t})^{n+1} + \triangledown \cdot (\rho^{n+1}\vec{\mathbf{U}}^*) + \triangledown \cdot \widetilde{J}^{n+1}}{\Delta t}. \tag{21}$$

Unlike the conventional Poisson equation for an incompressible multiphase flow [35], $\triangledown^2 P^{n+1}$ in Eq. (21) has a constant coefficient and there is no need to compute the variable coefficient matrices at each time step. This Poisson equation can be solved with a fast Poisson solver or direct methods. $\vec{\mathbf{U}}^{n+1}$ is then computed by solving Eq. (18).

2.3.2. Energy equation in Step 6

Generally, an energy equation is not essential for some multiphase flow simulations without phase change (e.g, wetting simulations) as the temperature variations are negligible. For the simulations with phase change, however, the energy equation is indispensable to determine the temperature field and the associated heat and mass fluxes. The energy equation (13) contains the product of material properties that are functions of the phase-field order parameters, such as the product of density and heat capacity ρC_p. We realised during this study that these products must be carefully determined. It has been already mentioned that each material property of the mixture is obtained through a linear interpolation of the phase-field order parameters (see Eq. (3) - (5)). In the same way, the heat capacity of the mixture is calculated as:

$$c_p(\phi, c) = \frac{1}{2}(\phi + 1) \cdot \left[(c + 1)c_{p2} - c_{p3} \right] - \frac{1}{2}(\phi - 1)c_{p1}. \tag{22}$$

In previous studies [17, 38], the product ρC_p in the energy equation is often computed as $\bar{\rho}\bar{C}_p = \rho(\phi, c)c_p(\phi, c)$. In this paper, we calculate it as $\rho C_p = \sum_{n=1}^{m} \rho_n C_{pn} V_n$, where m is the number of the phases and V_n is the volume fraction of each single phase. For three-phase flows we thus have:

$$\rho C_p = \rho_1 C_{p1} V_1 + \rho_2 C_{p2} V_2 + \rho_3 C_{p3} V_3, \tag{23}$$

where V_1, V_2 and V_3 are given as:

$$
\begin{aligned}
V_1 &= \frac{1 - \phi}{2}, \\
V_2 &= \frac{1 + \phi}{2}(1 + c), \\
V_3 &= \frac{1 + \phi}{2}(-c).
\end{aligned}
\tag{24}
$$

The use of Eq. (23) turned out to be more accurate than the direct multiplication of the density and heat capacity $\bar{\rho}\bar{C}_p$. We denote Eq. (23) as "average of products" and $\bar{\rho}\bar{C}_p$ as "product of averages". To demonstrate the difference between the two, here we provide a simple example: consider a volume of 1 m^3 with $\phi = 0.4$ and $c = 0$ filled with a mixture of water and air. The heat required to increase the mixture by $1°C$ is 2.93×10^6 J when computed with Eq. (23) and 2.06×10^6 J with $\bar{\rho}\bar{C}_p$. Hence, there is a large discrepancy between these two calculation methods, which will be further discussed in Section 4.2.

The algorithm used for the energy equation is the second-order implicit Crank-Nicolson scheme:

$$\frac{\partial(\rho C_p T)}{\partial t} = \frac{1}{2}(E^{n+1} + E^n) + \frac{\partial V_3}{\partial t}\rho_3 L, \tag{25}$$

where

$$E = -\nabla \cdot (\rho C_p T \vec{\mathbf{U}}) + \nabla \cdot (k \nabla T) + \Phi + \rho \vec{\mathbf{U}} \cdot g. \tag{26}$$

2.3.3. Correction of the ice velocity

We now consider Step 7 of the algorithm. While in the simulation the ice is formally treated as following the fluid governing equations, it is assumed here a solid phase and its numerical velocity should be reduced as much as possible. To achieve this goal, two procedures are followed during the computation: 1) a very large viscosity is specified for the ice (eg., 10^5 times of the viscosity of water); 2) at the end of every time step, the velocity of the ice is forced to be zero through the following correction

$$\vec{\mathbf{U}}_{cor}^{n+1} = \vec{\mathbf{U}}^{n+1}(mass_{water} + mass_{air})/(mass_{ice} + mass_{water} + mass_{air}). \tag{27}$$

The mass of the different phases can be computed by multiplying the volume fraction in Eq. (24) and the corresponding densities (e.g., $mass_{water} = \rho_2 V_2$). In this equation, the velocity of ice in the mixture is set to zero while the velocity of air and water remains unchanged. Therefore, the momentum of the mixture is not conserved, however the loss is very small. The corrected mixture velocity, $\mathbf{U}_{cor}^{n+1}$, will be used in the next time step. This correction is similar to the volume penalization method used in [39]. Note that for some specific problems, it might be enough to consider the ice as high-viscosity fluid [40] or a visco-plastic fluid [41, 42].

2.4. Discretization

2.4.1. Temporal discretization

A second-order explicit temporal discretization is used for the CH equation (Eq. (6)), AC equation (Eq. (9)) and NS equations (Eq. (12)). A generic expression for the time evolution of a variable φ is given by:

$$\frac{\partial \varphi}{\partial t} = f(\varphi), \tag{28}$$

where the function f incorporates any spatial discretization. The second-order temporal discretization is written as:

$$\frac{3\varphi^{n+1} - 4\varphi^n + \varphi^{n-1}}{2\Delta t} = 2f(\varphi^n) - f(\varphi^{n-1}). \tag{29}$$

Eq. (16) and (17) are discretized as:

$$\frac{3\rho^{n+1}\vec{\mathbf{U}}^* - 4\rho^n\vec{\mathbf{U}}^n + \rho^{n-1}\vec{\mathbf{U}}^{n-1}}{2\Delta t} = 2\mathrm{RU}^n - \mathrm{RU}^{n-1} \tag{30}$$

and

$$\frac{3\vec{\mathbf{U}}^{n+1} - 3\vec{\mathbf{U}}^*}{2\Delta t} = -\frac{1}{\rho^{n+1}} \nabla P^{n+1}. \tag{31}$$

The Poisson equation to solve the pressure is:

$$\nabla^2 P^{n+1} = \frac{3\frac{3\rho^{n+1} - 4\rho^n + \rho^{n-1}}{2\Delta t} + 3 \nabla \cdot (\rho^{n+1}\mathbf{U}^*) + 3 \nabla \cdot \widetilde{J}^{n+1}}{2\Delta t}. \tag{32}$$

To ensure the numerical stability, the time step Δt are restricted as follows [6, 43, 35]:

$$\begin{aligned}
\Delta t &= \frac{1}{2} min(\Delta t_v, \ \Delta t_s, \ \Delta t_c), \\
\Delta t_v &\sim \min\left[\frac{1}{4}\frac{(\Delta x)^2}{|\eta_1|}\right], \\
\Delta t_s &\sim \frac{1}{2}\sqrt{\frac{\rho_2}{\sigma_\phi}(\Delta x)^3}, \\
\Delta t_c &\sim min\left[\frac{\Delta x}{\left|\vec{\mathbf{U}}\right|}\right],
\end{aligned} \tag{33}$$

where Δt_v, Δt_s and Δt_c represents the estimation of time step constraint accounting for the stability condition on viscosity, surface tension and convection, respectively. For the three-phase simulations in Section 3, we have $\Delta t_c > \Delta t_v > \Delta t_s$ and thus the restriction is mainly imposed by the surface tension term in the CH equation. The main advantage of the explicit scheme is that it requires less memory and programming efforts. However, as high spatial resolution is essential to resolve the interface between different phases, a small Δt has to be used to ensure numerical stability [35, 44]. To enable a larger time step size, one can treat the surface tension term implicitly as in the method outlined in [45] and a semi-implicit method where the viscous terms are treated implicitly [46].

With the implicit Crank-Nicolson scheme, the energy equation is discretized as:

$$\frac{\partial(\rho C_p T)}{\partial t} = \frac{(\rho C_p)^{n+1}T^{n+1} - (\rho C_p)^n T^n}{\Delta t}, \tag{34}$$

where $\rho C_p = \sum_{n=1}^{m} \rho_n C_{pn} V_n$. Eq. (29) is used for $\partial c / \partial t$ in the energy equation:

$$\frac{\partial c}{\partial t} = \frac{3c^{n+1} - 4c^n + c^{n-1}}{2\Delta t}. \tag{35}$$

For a one-dimensional problem, the spatial discretization of the energy equation will generate a tridiagonal matrix and the Thomas algorithm is adopted to obtain the solution. The alternating-direction implicit (ADI) method can be used for two- and three-dimensional simulations.

2.4.2. Spatial discretization

In this section, the spatial discretizations are presented in detail. In the present work, all the discrete operators defined are second-order on a Cartesian staggered grid using the central difference scheme. The velocity is defined at the cell surface and all the other scalar parameters are located in the cell centre. Without loss of generality, a two-dimensional formulation is presented for simplicity; this can be extended to three dimensions or degraded to one dimension straightforwardly. For a two-dimensional problem, the cell centre is denoted as (x_i, y_j) and the cell face as $(x_{i+\frac{1}{2}}, y_j)$ or $(x_i, y_{j+\frac{1}{2}})$. We use $\mathbf{F}, \mathbf{G}$ and $\mathbf{H}$ to denote the vector parameters at the cell surface while the scalar parameters are denoted as $\mathcal{F}, \mathcal{G}$ and $\mathcal{H}$ at the cell centre. Therefore, a vector $\mathbf{F}$ defined at the cell surface $(x_{i+\frac{1}{2}}, y_j)$ is written as $\mathbf{F}^x_{i+\frac{1}{2},j}$ and x component as $F^x_{i+\frac{1}{2},j}$. For example, the x-component of the velocity $\vec{\mathbf{U}}$ at the surface $(x_{i+\frac{1}{2}}, y_j)$ is $U^x_{i+\frac{1}{2},j}$. Similarly, a scalar parameter at the cell centre is marked as $\mathcal{F}_{i,j}$, and Δx and Δy stand for the cell size along the x and y directions. $\mathbf{i}$ and $\mathbf{j}$ are the standard unit vectors for the x- and y-axes. The discrete operations implemented are central-difference interpolation, gradient terms, divergence terms and Laplace terms.

i) Central-difference interpolation

The x component of a vector at the cell surface is interpolated to the cell centre using the following central interpolation:

$$\mathbf{F}^x_{i,j} = \frac{\mathbf{F}^x_{i+\frac{1}{2},j} + \mathbf{F}^x_{i-\frac{1}{2},j}}{2}. \tag{36}$$

Similarly, a scalar defined at the cell centre is interpolated to the cell surface $(x_i, y_{j+\frac{1}{2}})$ as follows:

$$\mathcal{F}^y_{i,j+\frac{1}{2}} = \frac{\mathcal{F}_{i,j+1} + \mathcal{F}_{i,j}}{2}. \tag{37}$$

The interpolation of the parameters along the other axis is computed in the same manner.

ii) Discrete gradient

The discrete gradient of a scalar at the cell centre is defined as:

$$\nabla \mathcal{F}_{i,j} = \frac{\mathcal{F}_{i+1,j} - \mathcal{F}_{i-1,j}}{2\Delta x}\mathbf{i} + \frac{\mathcal{F}_{i,j+1} - \mathcal{F}_{i,j-1}}{2\Delta y}\mathbf{j}. \tag{38}$$

The convection term in Eq. (6), evaluated at the cell centre, is thus computed as:

$$[\mathbf{F} \cdot \nabla \mathcal{F}]_{i,j} = \frac{(F^x_{i+\frac{1}{2},j} + F^x_{i-\frac{1}{2},j})(\mathcal{F}_{i+1,j} - \mathcal{F}_{i-1,j})}{4\Delta x} + \frac{(F^y_{i,j+\frac{1}{2}} + F^y_{i,j-\frac{1}{2}})(\mathcal{F}_{i,j+1} - \mathcal{F}_{i,j-1})}{4\Delta y}. \tag{39}$$

iii) Discrete divergence

The divergence appears in the equations in two different forms, both evaluated at the cell centre. The first

$$[\nabla \cdot (\mathbf{F}\mathcal{F})]_{i,j} = \frac{F^x_{i+\frac{1}{2},j}(\mathcal{F}_{i+1,j} + \mathcal{F}_{i,j}) - F^x_{i-\frac{1}{2},j}(\mathcal{F}_{i-1,j} + \mathcal{F}_{i,j})}{2\Delta x} + \frac{F^y_{i,j+\frac{1}{2}}(\mathcal{F}_{i,j+1} + \mathcal{F}_{i,j}) - F^y_{i,j-\frac{1}{2}}(\mathcal{F}_{i,j-1} + \mathcal{F}_{i,j})}{2\Delta y}, \tag{40}$$

is used for the convection term in Eq. (9). The second expression,

$$\begin{aligned}
[\nabla \cdot (\mathcal{F} \nabla \mathcal{G})]_{i,j} = &\frac{(\mathcal{F}_{i+1,j} + \mathcal{F}_{i,j})\frac{\mathcal{G}_{i+1,j} - \mathcal{G}_{i,j}}{\Delta x} - (\mathcal{F}_{i-1,j} + \mathcal{F}_{i,j})\frac{\mathcal{G}_{i,j} - \mathcal{G}_{i-1,j}}{\Delta x}}{2\Delta x} + \\
&\frac{(\mathcal{F}_{i,j+1} + \mathcal{F}_{i,j})\frac{\mathcal{G}_{i,j+1} - \mathcal{G}_{i,j}}{\Delta y} - (\mathcal{F}_{i,j-1} + \mathcal{F}_{i,j})\frac{\mathcal{G}_{i,j} - \mathcal{G}_{i,j-1}}{\Delta y}}{2\Delta y},
\end{aligned} \tag{41}$$

is used for the diffusion term in the energy equation. These discrete formulations also apply when multiple scalars appear in the equation.

The divergence at the cell surface $(x_{i+\frac{1}{2}}, y_j)$ used in the NS equation is defined as:

$$
\begin{aligned}
[\nabla \cdot (\mathcal{F}\mathbf{F} \otimes \mathbf{F})]^x_{i+\frac{1}{2},j} =& \frac{1}{\Delta x}[\mathcal{F}_{i+1,j}\frac{1}{2}(\mathbf{F}^x_{i+\frac{3}{2},j} + \mathbf{F}^x_{i+\frac{1}{2},j}) \cdot \frac{1}{2}(\mathbf{F}^y_{i+1,j+\frac{1}{2}} + \mathbf{F}^y_{i+1,j-\frac{1}{2}}) \\
& - \mathcal{F}_{i,j}\frac{1}{2}(\mathbf{F}^x_{i-\frac{1}{2},j} + \mathbf{F}^x_{i+\frac{1}{2},j}) \cdot \frac{1}{2}(\mathbf{F}^y_{i,j+\frac{1}{2}} + \mathbf{F}^y_{i,j-\frac{1}{2}})] \\
& + \frac{1}{\Delta y}[\frac{1}{4}(\mathcal{F}_{i,j} + \mathcal{F}_{i,j+1} + \mathcal{F}_{i+1,j+1} + \mathcal{F}_{i+1,j})\frac{1}{2}(\mathbf{F}^x_{i+\frac{1}{2},j} + \mathbf{F}^x_{i+\frac{1}{2},j+1}) \cdot \frac{1}{2}(\mathbf{F}^y_{i,j+\frac{1}{2}} + \mathbf{F}^y_{i+1,j+\frac{1}{2}}) \\
& - \frac{1}{4}(\mathcal{F}_{i,j} + \mathcal{F}_{i,j} + \mathcal{F}_{i,j-1} + \mathcal{F}_{i+1,j-1})\frac{1}{2}(\mathbf{F}^x_{i+\frac{1}{2},j} + \mathbf{F}^x_{i+\frac{1}{2},j-1}) \cdot \frac{1}{2}(\mathbf{F}^y_{i,j-\frac{1}{2}} + \mathbf{F}^y_{i+1,j-\frac{1}{2}})].
\end{aligned}
\tag{42}
$$

The divergence at the cell surface $(x_{i+\frac{1}{2}}, y_j)$ used in the viscous terms is instead defined as:

$$
\begin{aligned}
[\nabla \cdot (\mathcal{F}(\nabla \mathbf{F})^T)]^x_{i+\frac{1}{2},j} =& \frac{1}{\Delta x}[\mathcal{F}_{i+1,j}\frac{F^x_{i+\frac{3}{2},j} - F^x_{i+\frac{1}{2},j}}{\Delta x} - \mathcal{F}_{i,j}\frac{F^x_{i+\frac{1}{2},j} - F^x_{i-\frac{1}{2},j}}{\Delta x}] \\
& + \frac{1}{4\Delta y}[(\mathcal{F}_{i,j} + \mathcal{F}_{i+1,j} + \mathcal{F}_{i,j+1} + \mathcal{F}_{i+1,j+1})\frac{F^y_{i+1,j+\frac{1}{2}} - F^y_{i,j+\frac{1}{2}}}{\Delta x} - \\
& (\mathcal{F}_{i,j} + \mathcal{F}_{i+1,j} + \mathcal{F}_{i,j-1} + \mathcal{F}_{i+1,j-1}) \cdot \frac{F^y_{i+1,j-\frac{1}{2}} - F^y_{i,j-\frac{1}{2}}}{\Delta x}].
\end{aligned}
\tag{43}
$$

iv) Discrete Laplace operator

The discrete Laplace operator at the cell centre is here defined as:

$$
\nabla^2 \mathcal{F}_{i,j} = \frac{\mathcal{F}_{i+1,j} + \mathcal{F}_{i-1,j} - 2\mathcal{F}_{i,j}}{(\Delta x)^2} + \frac{\mathcal{F}_{i,j+1} + \mathcal{F}_{i,j-1} - 2\mathcal{F}_{i,j}}{(\Delta y)^2}.
\tag{44}
$$

3. Description of the test case

To validate the proposed scheme, a one-dimensional test case using staggered grid (Fig. 2) is presented. The one-dimensional simulation is capable to represent the essential phenomena concerned including volume expansion of ice and movement of the water-air interface. The two- and three-dimensional simulations will be shown in future work. The phase-field order parameter ϕ, c, density ρ, material properties (e.g., C_p, k, η) and pressure P are stored at the cell centre. The velocity is set normal to the cell face between two consecutive cells. The total length of the domain is $l = 4mm$ and the domain is equally split into N cells ($i = 1 \sim N$).
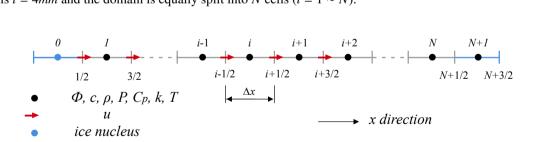

Fig. 2: One-dimensional schematic of the staggered grid arrangement.

Two boundary cells ($i = 0$, $i = N + 1$) are added to the computational domain. The left boundary is assumed to be a cold solid wall where the icing process is initiated. The right boundary is set as a vent with constant pressure which permits the flow to enter or leave the computational domain. At the left boundary cell ($i = 0$) a Neumann boundary condition is used for pressure and a Dirichlet boundary condition is used for velocity, which gives:

$$
P_0 = P_1, u_{\frac{1}{2}} = 0 \, m/s.
\tag{45}
$$

At the right boundary, a Dirichlet boundary condition is used for pressure and a Neumann boundary condition for velocity, thus at $N + 1$, we have

$$P_{N+1} = 0\, Pa, u_{N+\frac{3}{2}} = u_{N+\frac{1}{2}}. \tag{46}$$

At the right boundary, $\phi = 1$ and the gradient of ϕ equals zero at the left boundary. The initial condition of the phase-field order parameter ϕ is given by the following hyperbolic tangent function,

$$\phi = -tanh(\frac{x - \frac{l}{2}}{\sqrt{2}\xi_\phi}), \tag{47}$$

with x the axial distance from the wall. At the left boundary, $c = -1$ is the ice nuclear while $c = 0$ in all the other cells. During the computation, $\frac{\partial c}{\partial t}$ will be forced to be zero where the temperature is above 0°C. By this, it can be guaranteed that no ice will form above the melting point. The temperature of the left boundary is fixed whereas the right boundary is adiabatic. The value of $\vec{U}^*$ at the left boundary is fixed to 0 and the zero gradient condition is used at the right boundary.

The values of the physical parameters used in the simulations are listed as follows: $M_\phi = 5.2 \times 10^{-10} N \cdot s \cdot m^{-1}$, $g = 9.8\, m/s^2$, $\sigma_\phi = 0.0727\, N/m$, $\xi_\phi = 8.0 \times 10^{-5}\, m$, $M_c = 2.0 \times 10^{-5} N \cdot s \cdot m^{-1}$, $\sigma_c = 0.0317\, N/m$, $\xi_c = 2.64 \times 10^{-4}\, m$, $L = 334000\, J/Kg$, $T_M = 273.15\, K$, $u_{ref} = 1m/s$, $l_{ref} = l/5$. The value of the surface tension coefficient between the water and ice is obtained from an experimental study [47]. The accurate value of the mobility varies with the material and can be determined experimentally or through molecular dynamics simulations. The magnitude of the mobility is 10^{-9} in the dynamic wetting model for water in [48] while the magnitude varies from 10^{-5} to 10^{-11} in [49]. The other material properties of air, water and ice are summarised in Table 1. Regarding the viscosity of ice, it is proved that 10^5 times of the water viscosity is sufficient to suppress the motion inside the ice during the computation.

Table 1: Material properties of air, water and ice.

Phase	Density (kg/m^3)	Viscosity ($Pa \cdot s$)	Thermal conductivity ($W/(m \cdot K)$)	Heat capacity $J/(K \cdot kg)$
air	1.2	1.6e-5	0.0209	1.0
water	998	1.0e-3	0.5918	4200
ice	898	100	2.25	2018

Table 2 report the x position of the water-air interface for different spatial resolutions at time $t = 20s$. $\Delta t = 1.0 \times 10^{-7}s$ is adopted. The results converges to 4 significant figures at $N = 400$. $N = 400$ is used in the temporal resolution test and when Δt is halved from $8.0 \times 10^{-7}s$ to $5.0 \times 10^{-8}s$, there is no change in the first four significant figures. Based on these observations, $N = 400$ and $\Delta t = 1.0 \times 10^{-7}s$ are selected for the following simulations.

Table 2: Position of the water-air interface.

Grid	Water-air interface
80	1.630mm
160	1.644mm
240	1.649mm
320	1.651mm
400	1.653mm
480	1.653mm

The convergence of the simulation is evaluated by the residual of the continuity equation, which is not directly solved. This is computed as:

$$Residual = \sqrt{\sum_{i=1}^{N} [\frac{\partial \rho_i}{\partial t} + \triangledown \cdot (\rho \vec{U} + \widetilde{J})_i]^2 / N}. \tag{48}$$

During the computation, the magnitude of the residual is in the range $10^{-15} \sim 10^{-13}$.

4. Convergence and validation

In this section, two test cases are presented to validate the proposed scheme. The first one adopts the artificial solutions which is infinitely differentiable to validate the discretization is second-order accurate in space. The second test simulates the icing of supercooled water and it is compared against the analytical solution, where the modelling of the three-phase flow is justified.

4.1. Convergence rates

We demonstrate the spatial convergence rate of the numerical scheme in Section 2.3 using manufactured analytical solutions. The simulation domain $\Omega = (x, t) : 0 \leqslant x \leqslant 2\pi, 0 \leqslant t \leqslant 1$ and the manufactured solutions are:

$$\begin{cases} u = sin(x)cos(t), \\ \phi = cos(x)sin(t), \\ c = sin(x)cos(t), \\ P = cos(x)sin(t), \\ T = sin(x)sin(t). \end{cases} \tag{49}$$

A source term is added to each equation ((6), (9), (11)-(13)) to make the solutions satisfy the governing equations. For example, the source term in the continuity equation (11) is computed by substituting the analytical solutions into:

$$S_{mass} = \frac{\partial \rho}{\partial t} + \triangledown \cdot (\rho \vec{U} + \widetilde{J}). \tag{50}$$

Density, viscosity and thermal conductivity are computed using Eq. (3)-(5) with the analytical solutions Eq. (49). The other source terms are computed in the same way. Dirichlet conditions for the phase-field order parameters, velocity and pressure are computed based on the analytical solutions. We employ the following values for the parameters in the spatial convergence rate tests: $M_\phi = 1 \times 10^{-3}$, $g = 1$, $\sigma_\phi = 2\sqrt{2}/3$, $\xi_\phi = 1$, $M_c = 1 \times 10^{-2}$, $\sigma_c = 1$, $\xi_c = 1$, $L = 0.2$, $T_M = 1$, $u_{ref} = 1$, $l_{ref} = 1$, $\rho_1 = 1$, $\rho_2 = 2$, $\rho_3 = 3$, $Cp_1 = 1$, $Cp_2 = 1/2$, $Cp_3 = 1/3$, $k_1 = 1$, $k_2 = 2$, $k_3 = 3$.

The scheme in Section 2.4 is employed to discretize the equation system. To test the spatial convergence rate, a sufficiently small fixed time step size $\Delta t = 10^{-6}$ is used to guarantee that the overall error is dominated by the spatial discretization. The initial solutions are set according to the analytical solution at $t = 0$ and $t = -10^{-6}$. We systematically refine the size of Δx, for each resolution, integrate the result from $t = 0$ to $t = 1$. The L_2 error of a variable is defined as the root mean square of the difference between the computed value ψ and the analytical value Ψ in the domain Ω:

$$L_2 = \sqrt{\frac{1}{n} \sum_{i=1}^{n} (\psi_i - \Psi_i)^2}. \tag{51}$$

The L_∞ error is the maximum of the pointwise difference $|\psi_i - \Psi_i|$. The L_2 and L_∞ error for different flow parameters as a function of Δx are displayed in Fig. 3 to confirm the second-order spatial convergence rate of our numerical scheme.

4.2. Solidification of supercooled water

Another test case was designed to validate the proposed numerical scheme: the solidification process of super-cooled water on a one-dimensional grid. The domain is initially filled with supercooled water of constant temperature. The icing process starts from the left boundary and the water-ice interface moves towards the right boundary. In this case, the left and right boundary are adiabatic to guarantee that the total internal energy is conserved. As latent heat is released by water during the solidification, the temperature of the water-ice mixture increases. The icing process will cease when the temperature of the mixture reaches $0°C$. Under this circumstance, the whole flow field reaches thermal equilibrium and the temperature is uniform everywhere. It is expected that a lower supercooling temperature leads to the formation of more ice in the final state. An exact relation between the supercooling temperature and the mass of ice can be obtained for the equilibrium state. As the mass and the heat capacity of air is very small compared with that of ice and water, the influence of air on the ice mass is ignored. The conservation of the internal energy leads to:
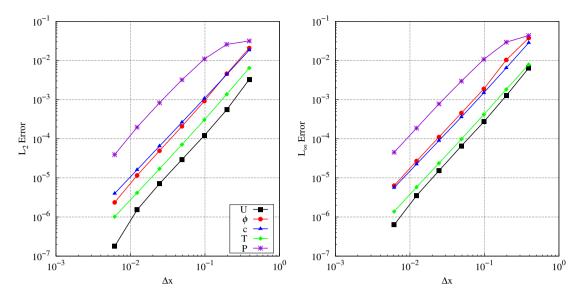
11

Fig. 3: Spatial convergence rate: L_2 (left) and L_∞ errors (right) of different flow parameters.

$$M_{water} \cdot T_c \cdot C_{p2} = m_{ice} \cdot L, \tag{52}$$

where, M_{water} is the total mass of the supercooled water at the initial state; T_c is the supercooling temperature defined as the temperature difference between the supercooled water and the melting point. The ratio between the ice mass and ther supercooled water m_{ice}/M_{water} is therefore proportional to the supercooling temperature of the water.

The comparison between the analytical solution above (black line) and the results of our simulations (red dots) is displayed in Fig. 4. The results obtained using the "product of averages", $\bar{\rho}\bar{C}_p$ (Eq. (23)), in the energy equation are also shown in this figure. Clearly, adopting Eq. (23) the data accurately matches the analytical solution, while using $\bar{\rho}\bar{C}_p$ leads to a discrepancy between the simulation and the analytical solution. This error increases as the supercooling temperature becomes larger.
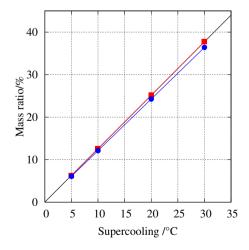

Fig. 4: Mass ratio for different supercooling conditions: — analytical solution; —■— present results; —●— results with $\bar{\rho}\bar{C}_p$.

12

5. Parametric study

As validation, we have considered only the final equilibrium state in Section 4.2. Here, we consider the complete one-dimensional icing process for the values of the physical parameters listed in Section 3. Fig. 5 displays the evolution of the water-ice and the water-air interfaces in the (x-t) plane with time as ordinate ($t = 0 \sim 100s$) and the index of the grid points in abscissa. The red region in the figure represents the liquid water and the blue region denotes the air. The icing is indicated by the growth of the green region ($c = -1$), which starts from the left boundary. In this case, the temperature at the left boundary is $T_{wall} = -5°C$ and the initial temperature of the water and air is $T_o = 0.2°C$. Most of the water has become ice after $t = 70s$. The curvature of the water-ice interface in Fig. 5 indicates that the icing speed gradually decreases as the solidification front moves forward. As the solidification of water is accompanied by volume expansion, the interface between water and air is pushed towards the right boundary and the air is squashed out of the simulation domain across the right boundary.
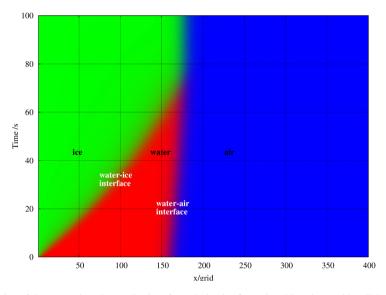

Fig. 5: Time evolution of the water-air and water-ice interfaces during ice formation driven by a cold wall, here the left boundary.

In Fig. 6 we show the evolution of the temperature in the (x-t) plane with time as ordinate ($t = 0 \sim 100s$) and the index of the grid points in abscissa. The water-ice and the water-air interfaces are marked with dashed lines. Initially ($0 \sim 20s$) the ice layer is thin and the released latent heat from icing is transferred to the cold wall. Consequently the temperature of the whole domain keeps decreasing. However, as the icing front moves away from the wall, the thicker ice layer obstructs the removal of the released heat and the temperature near the icing front is higher than its neighbouring region. At around $t = 70s$, most of the water has turned into ice. In absence of the heating effect of the icing process, the temperature of the air drops very fast due to its low heat capacity and the temperature of the whole domain becomes almost uniform after $t = 80s$.

We display in Fig. 7 the initial profiles and the final solutions at $t = 500s$ of the order parameters ϕ, c and temperature. The shape of ϕ is unchanged during the motion and the water-ice interface, $c = 0$, locates exactly at the boundary of pure air ($\phi = -1$). The initial volume of water occupies 160 cells and the final volume of ice is about 177.8 cells (indicated by $\phi = 0$). The volume change from water to ice is in line with the water-ice density ratio, which proves that the volume expansion of the icing process is accurately captured during the computation.

A parametric study is then carried out to investigate the influence of the physical parameters (solidification mobility M_c, wall temperature T_0 and thickness of the water-ice interface ξ_c). Firstly, different values of the mobility M_c are tested while all the other parameters remain constant as presented in Section 3. The values of c and temperature at $t = 5s$ are displayed in Fig. 8. The evolution of c is significantly affected by the mobility, which is used to describe the atomic diffusion: a larger mobility speeds up the icing process. The temperature of the flow field is mainly determined by two factors: the heat conduction to the the cold wall, which lowers the temperature of the flow field, and the release of latent heat during solidification, which, conversely, locally increases the temperature. As the icing process is faster with larger mobility, the heating from the latent heat overcomes the cooling from the heat conduction and,
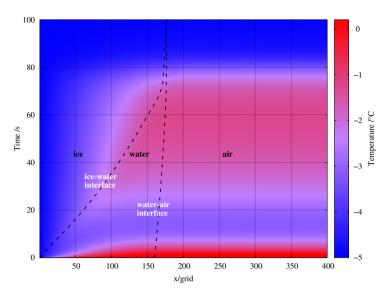
Fig. 6: Time evolution of the temperature during ice formation driven by a cold wall, here the left boundary.
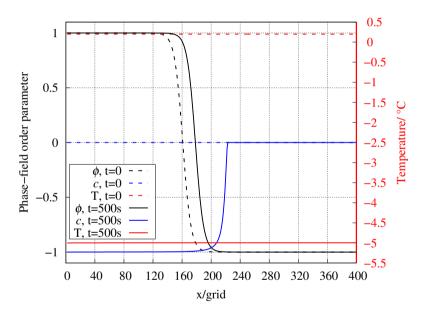

Fig. 7: Initial and final solution of the phase-field parameters and temperature from the simulation of ice formation driven by a cold wall.

consequently, the overall temperature of the flow field becomes higher. It is also noted that the speed of the ice front is approximately proportional to the mobility. It is considered that the accurate value of the mobility can be determined by tuning the icing speed against measured experimental values.

The wall temperature affects the icing speed in two ways: 1) a lower wall temperature can promote the heat removal and hence reduce the temperature of the water below melting point faster as no icing can form above $0°C$; 2) once the water drops below $0°C$, the water supercooling can accelerate the ice formation according to Eq. (10). To examine these effects, results obtained with different wall temperature at time $t = 20s$ are depicted in Fig. 9. Here, we observe that the temperature is slightly higher at the solidification front than in the neighbouring region due to the release of latent heat. This occurs when the icing speed is fast and the heat conduction to diffuse the heat released during the phase change is slow .

In the simulations using the phase-field method, the thickness of the interface is inevitably set to values larger than those known for the system modelled [1, 50], so that the spatial resolution needed to resolve the interface is reduced.
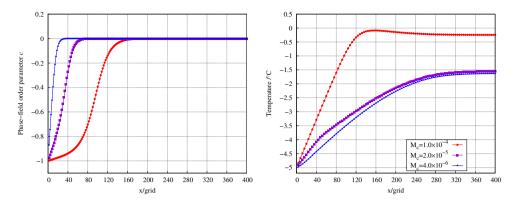
14

Fig. 8: Influence of mobility on the profiles of phase field order parameter (left) and temperature (right) extracted at $t = 5s$.
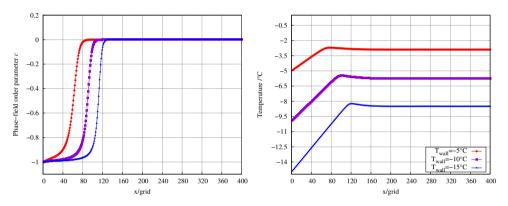

Fig. 9: Influence of wall temperature on the profiles of phase field order parameter (left) and temperature (right) extracted at $t = 20s$.
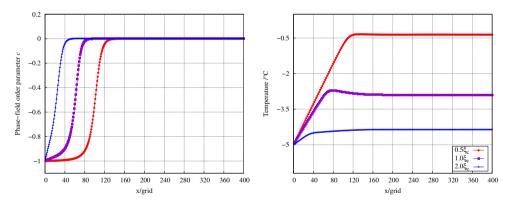

Fig. 10: Influence of water-ice interface thickness on the profiles of phase field order parameter (left) and temperature (right) extracted at $t = 20s$.

Taking the icing as an example, the measured thickness of the ice-water interface is around 1 *nm* and it varies with the level of supercooling [51, 52, 18]. Here, we test three different thicknesses of the water-ice interface and display the numerical solutions at time $t = 20s$ in Fig. 10. The data indicate that a wider interface reduces the solidification speed and hence the release of the latent heat. Hence, the temperature of the flow field is lower for thicker interfaces. As a result, the icing speed will be under-predicted when the spatial resolution of the interface is low, because the interface is smoothed. As the interface thickness used in any simulation is doomed to deviate from the true value, this must be carefully adjusted to accurately model the ice formation over time.

Another important issue remains unproved is the uniqueness of the solution for the equation system. The computations with disturbances of different amplitudes in the velocity U and temperature T are conducted. The initial flow
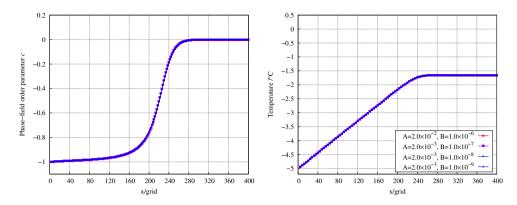
Fig. 11: Profiles of phase field order parameter (left) and temperature (right) extracted at $t = 80s$ with disturbances.

field with disturbance is defined as:

$$T = T_o + A \cdot sin(\frac{5x}{2\pi l}), \tag{53}$$

$$U = U_o + B \cdot sin(\frac{5x}{2\pi l}), \tag{54}$$

where A and B denote the amplitude of the disturbance in temperature and velocity, respectively. The mobility, interface thickness and the temperature $T_o = 0.2°C$ of the initial flow field are exactly the same as the case in Fig. 5. Different values of A up to $0.02°C$ and B up to $1.0 \times 10^{-6}m/s$ are tested, where the largest velocity in the flow field during icing is around $1.0 \times 10^{-5}m/s$. It is found that the final solutions are exactly the same in presence of the disturbances, as shown in 11 at $t = 80s$. This demonstrates numerically the robustness of the computational scheme and the uniqueness of the solution over the parameters considered.

6. Conclusions and discussion

In this paper, we propose a numerical model and its implementation to solve a three-phase flows with phase change. The Cahn-Hillard equation, Allen-Cahn equation, Navier-Stokes equation and energy equation are combined to simulate the icing of water in an inert gas. The main features of the method can be summarised as follows:

1) By introducing two different phase-field order parameters, we can track the motion of the interfaces between water-ice and water-air simultaneously. We assume solidification occurs in the liquid region, and this drives also the motion of the water-air interface owing to the density difference between water and ice. At the same time, we neglect in this model evaporation of the liquid into the gas. We consider this work as the first study where solidification with density change is modelled in three-phase flows.

2) A Poisson equation with a constant coefficient is derived by combining the momentum and continuity equations, which requires no pre-conditioning. This enables us to use fast Poisson solvers of reduced computational cost. We prove that the projection method can be successfully applied in the simulation of icing, where the solenoidal (divergence-free) condition is no longer valid.

3) Regarding the energy equation for the ternary flow, it is pointed out and proved in the numerical tests that a significant error is generated when an inappropriate averaging of the material properties at the interface is adopted. The linear constitutive equation based on the phase-field order parameters commonly used for the fluid material properties is not a proper choice in our problem.

4) The second-order spatial accuracy of the discretization is validated against ad hoc analytical solutions. A one-dimensional test case of the supercooled water solidification is employed to demonstrate the accuracy of the method. The simulations successfully capture the motion of the water-air interface due to the volume expansion caused by the icing.

5) The parametric study conducted shows how the physical parameters influence the icing process, which indicates essential tuning is indispensable for the accurate modeling of the physical phenomena. Simulations with flow disturbance are carried out to demonstrate the robustness of the proposed numerical scheme.

16

In future work, the thermodynamically consistent scheme [53] will be adopted, and the implementation will be extended to two- and three-dimensions, following the proposed numerical strategy. As the icing process of a water droplet involves dynamic wetting on a solid surface, a suitable wall boundary condition will be needed to account for contact line motion in the presence of phase change. Other extensions of our model, incorporating additional physical features, are the modelling of vapor in the gas phase and the influence of air flow on the ice formation and on the final shape of the solid region.

Acknowledgments

7. Appendix

7.1. Derivation of the Poisson equation

In this section, we present this derivation of the Poisson equation in Cartesian coordinate. The continuity equation in Cartesian coordinate is

$$\frac{\partial \rho^{n+1}}{\partial t} + \frac{\partial \rho^{n+1}}{\partial x} u^{n+1} + \frac{\partial \rho^{n+1}}{\partial y} v^{n+1} + \frac{\partial \rho^{n+1}}{\partial z} w^{n+1} + \rho^{n+1} \left[\frac{\partial u^{n+1}}{\partial x} + \frac{\partial v^{n+1}}{\partial y} + \frac{\partial w^{n+1}}{\partial z} \right] + \widetilde{J}^{n+1} = 0 \qquad (55)$$

and Eq. (18) is:

$$
\begin{aligned}
u^{n+1} &= u^* - \frac{\Delta t}{\rho^{n+1}} \frac{\partial P^{n+1}}{\partial x}, \\
v^{n+1} &= v^* - \frac{\Delta t}{\rho^{n+1}} \frac{\partial P^{n+1}}{\partial y}, \\
w^{n+1} &= w^* - \frac{\Delta t}{\rho^{n+1}} \frac{\partial P^{n+1}}{\partial z},
\end{aligned}
\qquad (56)
$$

and Eq. (19) can be written as:

$$
\begin{aligned}
\frac{\partial u^{n+1}}{\partial x} + \frac{\partial v^{n+1}}{\partial y} + \frac{\partial w^{n+1}}{\partial z} &= \frac{\partial u^*}{\partial x} + \frac{\partial v^*}{\partial y} + \frac{\partial w^*}{\partial z} + \frac{\Delta t}{(\rho^{n+1})^2} \cdot \frac{\partial \rho^{n+1}}{\partial x} \cdot \frac{\partial P^{n+1}}{\partial x} + \\
\frac{\Delta t}{(\rho^{n+1})^2} \cdot \frac{\partial \rho^{n+1}}{\partial y} \cdot \frac{\partial P^{n+1}}{\partial y} &+ \frac{\Delta t}{(\rho^{n+1})^2} \cdot \frac{\partial \rho^{n+1}}{\partial z} \cdot \frac{\partial P^{n+1}}{\partial z} - \frac{\Delta t}{\rho^{n+1}} \cdot \left(\frac{\partial^2 P^{n+1}}{\partial x^2} + \frac{\partial^2 P^{n+1}}{\partial y^2} + \frac{\partial^2 P^{n+1}}{\partial z^2} \right).
\end{aligned}
\qquad (57)
$$

In Eq. (19), $\Delta t \nabla \cdot (\frac{1}{\rho^{n+1}} \nabla P^{n+1})$ is denoted in Cartesian coordinate:

$$
\begin{aligned}
\Delta t \nabla \cdot (\frac{1}{\rho^{n+1}} \nabla P^{n+1}) &= \Delta t \cdot \left[\nabla \frac{1}{\rho^{n+1}} \cdot \nabla \rho^{n+1} + \frac{1}{\rho^{n+1}} \nabla^2 P^{n+1} \right] = \\
\Delta t \left[\frac{\partial}{\partial x}(\frac{1}{\rho^{n+1}}) \cdot \frac{\partial P^{n+1}}{\partial x} \right. &+ \frac{\partial}{\partial y}(\frac{1}{\rho^{n+1}}) \cdot \frac{\partial P^{n+1}}{\partial y} + \frac{\partial}{\partial z}(\frac{1}{\rho^{n+1}}) \cdot \frac{\partial P^{n+1}}{\partial z} + \frac{1}{\rho^{n+1}} \cdot \left(\frac{\partial^2 P^{n+1}}{\partial x^2} + \frac{\partial^2 P^{n+1}}{\partial y^2} + \frac{\partial^2 P^{n+1}}{\partial z^2} \right) \right] \\
&= -\frac{\Delta t}{(\rho^{n+1})^2} \frac{\partial \rho^{n+1}}{\partial x} \cdot \frac{\partial P^{n+1}}{\partial x} - \frac{\Delta t}{(\rho^{n+1})^2} \frac{\partial \rho^{n+1}}{\partial y} \cdot \frac{\partial P^{n+1}}{\partial y} - \frac{\Delta t}{(\rho^{n+1})^2} \frac{\partial \rho^{n+1}}{\partial z} \cdot \frac{\partial P^{n+1}}{\partial z} + \frac{\Delta t}{\rho^{n+1}} \cdot \left(\frac{\partial^2 P^{n+1}}{\partial x^2} + \frac{\partial^2 P^{n+1}}{\partial y^2} + \frac{\partial^2 P^{n+1}}{\partial z^2} \right) \\
&= -\frac{\Delta t}{(\rho^{n+1})^2} \cdot \frac{\partial \rho^{n+1}}{\partial x} \cdot \frac{\partial P^{n+1}}{\partial x} - \frac{\Delta t}{(\rho^{n+1})^2} \cdot \frac{\partial \rho^{n+1}}{\partial y} \cdot \frac{\partial P^{n+1}}{\partial y} - \frac{\Delta t}{(\rho^{n+1})^2} \cdot \frac{\partial \rho^{n+1}}{\partial z} \cdot \frac{\partial P^{n+1}}{\partial z} \\
&+ \frac{\Delta t}{\rho^{n+1}} \cdot \left(\frac{\partial^2 P^{n+1}}{\partial x^2} + \frac{\partial^2 P^{n+1}}{\partial y^2} + \frac{\partial^2 P^{n+1}}{\partial z^2} \right),
\end{aligned}
$$

$$(58)$$

substitute Eq. (57) and (56) into Eq. (55), we will finally get the Cartesian form of the Eq. (21):

$$
\begin{aligned}
\frac{\partial^2 P^{n+1}}{\partial x^2} + \frac{\partial^2 P^{n+1}}{\partial y^2} + \frac{\partial^2 P^{n+1}}{\partial z^2} &= \frac{1}{\Delta t}\left[\frac{\partial \rho^{n+1}}{\partial t} + \frac{\partial(\rho^{n+1}u^*)}{\partial x} + \frac{\partial(\rho^{n+1}v^*)}{\partial y} + \frac{\partial(\rho^{n+1}w^*)}{\partial z}\right] \\
&= \frac{1}{\Delta t}\left[\frac{\partial \rho^{n+1}}{\partial t} + \frac{\partial \rho^{n+1}}{\partial x}\cdot u^* + \frac{\partial \rho^{n+1}}{\partial y}\cdot v^* + \frac{\partial \rho^{n+1}}{\partial z}\cdot w^* + \rho^{n+1}(\frac{\partial u^*}{\partial x} + \frac{\partial v^*}{\partial y} + \frac{\partial w^*}{\partial z}) + \nabla\cdot\widetilde{J}^{n+1}\right].
\end{aligned}
\tag{59}
$$

7.2. Preliminary Two-dimensional tests

We have performed a few preliminary two-dimensional tests and a wetting simulation is briefly introduced here. It is found that when the density ratio between the liquid and the gas is large (for water and air, it is around 1000:1), the interface is less stable and the velocity across the interface is significantly larger than the real physical process. To stabilise the water-air interface, the Poisson equation is slightly modified to damp the interface velocity:

$$
\nabla^2 P^{n+1} = \frac{(\frac{\partial \rho}{\partial t})^{n+1} + |\varphi|\cdot \vec{\mathbf{U}}^* \cdot \nabla \rho^{n+1} + \rho^{n+1}\nabla\cdot\vec{\mathbf{U}}^* + \nabla\cdot\widetilde{J}^{n+1}}{\Delta t}.
\tag{60}
$$

while all the other procedures of the computation remain the same.

Fig. 12 shows the two-dimensional tests of the wetting process of a water droplet on a hydrophilic surface. In the test, a water droplet which is initially stationary and in contact with the surface, starts to wet the surface driven by gravity and the surface tension. The computational domain is $4mm \times 4mm$ and is discretized by 400×400 cells. The left boundary and right boundary is set as no-slip wall. The top boundary is set as outlet/inlet where the gradient of velocity is zero. Dirichlet boundary condition is used for the static pressure. is The generalized Navier slip boundary condition for moving contact lines is adopted at the bottom wall [54]. The contact angle between the water and the surface is 45 degrees. The physical parameters (e.g., density, viscosity, and heat capacity) are in accordance with the one-dimensional tests.
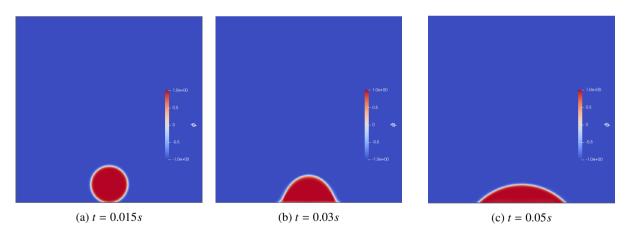

(a) $t = 0.015s$ (b) $t = 0.03s$ (c) $t = 0.05s$

Fig. 12: Wetting process of a water droplet on a hydrophilic surface.

References

[1] R. Qin, H. Bhadeshia, Phase field method, Materials science and technology 26 (2010) 803–811.

[2] L.-Q. Chen, Phase-field models for microstructure evolution, Annual review of materials research 32 (2002) 113–140.

[3] C. W. Hirt, B. D. Nichols, Volume of fluid (vof) method for the dynamics of free boundaries, Journal of computational physics 39 (1981) 201–225.

[4] C. Le Bot, S. Vincent, E. Arquis, Impact and solidification of indium droplets on a cold substrate, International Journal of Thermal Sciences 44 (2005) 219–233.

[5] J. A. Sethian, P. Smereka, Level set methods for fluid interfaces, Annual review of fluid mechanics 35 (2003) 341–372.

[6] M. Sussman, P. Smereka, S. Osher, et al., A level set approach for computing solutions to incompressible two-phase flow (1994).

[7] S. O. Unverdi, G. Tryggvason, A front-tracking method for viscous, incompressible, multi-fluid flows (1992).

[8] T. V. Vu, G. Tryggvason, S. Homma, J. C. Wells, Numerical investigations of drop solidification on a cold plate in the presence of volume change, International Journal of Multiphase Flow 76 (2015) 73–85.

[9] Q. Zhang, T.-Z. Qian, X.-P. Wang, Phase field simulation of a droplet impacting a solid surface, Physics of Fluids 28 (2016) 022103.

[10] H. Yu, X. Yang, Numerical approximations for a phase-field moving contact line model with variable densities and viscosities, Journal of Computational Physics 334 (2017) 665–686.

[11] N. Takada, M. Misawa, A. Tomiyama, A phase-field method for interface-tracking simulation of two-phase flows, in: Fluids Engineering Division Summer Meeting, volume 41995, 2005, pp. 259–264.

[12] D. Jacqmin, Calculation of two-phase navier–stokes flows using phase-field modeling, Journal of Computational Physics 155 (1999) 96–127.

[13] J. Shen, X. Yang, A phase-field model and its numerical approximation for two-phase incompressible flows with different densities and viscosities, SIAM Journal on Scientific Computing 32 (2010) 1159–1179.

[14] R. Kobayashi, Modeling and numerical simulations of dendritic crystal growth, Physica D: Nonlinear Phenomena 63 (1993) 410–423.

[15] I. Steinbach, Phase-field models in materials science, Modelling and simulation in materials science and engineering 17 (2009) 073001.

[16] J.-Q. Li, T.-H. Fan, T. Taniguchi, B. Zhang, Phase-field modeling on laser melting of a metallic powder, International Journal of Heat and Mass Transfer 117 (2018) 412–424.

[17] D. Juric, G. Tryggvason, Computations of boiling flows, International journal of multiphase flow 24 (1998) 387–410.

[18] T. U. Kaempfer, M. Plapp, Phase-field modeling of dry snow metamorphism, Physical Review E 79 (2009) 031502.

[19] D. M. Anderson, G. B. McFadden, A. A. Wheeler, A phase-field model of solidification with convection, Physica D: Nonlinear Phenomena 135 (2000) 175–194.

[20] B. Nestler, A. A. Wheeler, L. Ratke, C. Stöcker, Phase-field model for solidification of a monotectic alloy with convection, Physica D: Nonlinear Phenomena 141 (2000) 133–154.

[21] T. Suzuki, M. Ode, S. G. Kim, W. T. Kim, Phase-field model of dendritic growth, Journal of Crystal Growth 237 (2002) 125–131.

[22] Z. Bi, R. F. Sekerka, Phase-field model of solidification of a binary alloy, Physica A: Statistical Mechanics and its Applications 261 (1998) 95–106.

[23] F. Tavakoli, S. H. Davis, H. P. Kavehpour, Freezing of supercooled water drops on cold solid substrates: initiation and mechanism, Journal of Coatings Technology and Research 12 (2015) 869–875.

[24] L. Huang, Z. Liu, Y. Liu, Y. Gou, L. Wang, Effect of contact angle on water droplet freezing process on a cold flat surface, Experimental thermal and fluid science 40 (2012) 74–80.

[25] G. I. Tóth, W. Ma, Phase-field modelling of the effect of density change on solidification revisited: Model development and analytical solutions for single component materials, Journal of Physics: Condensed Matter 32 (2020) 205402.

[26] Y. Sun, C. Beckermann, Diffuse interface modeling of two-phase flows based on averaging: mass and momentum equations, Physica D: Nonlinear Phenomena 198 (2004) 281–308.

[27] Z. Guo, P. Lin, A thermodynamically consistent phase-field model for two-phase flows with thermocapillary effects, Journal of Fluid Mechanics 766 (2015) 226–271.

[28] J. Kim, Phase field computations for ternary fluid flows, Computer methods in applied mechanics and engineering 196 (2007) 4779–4788.

[29] F. Boyer, C. Lapuerta, S. Minjeaud, B. Piar, M. Quintard, Cahn–hilliard/navier–stokes model for the simulation of three-phase flows, Transport in Porous Media 82 (2010) 463–483.

[30] J. Kim, Phase-field models for multi-component fluid flows, Communications in Computational Physics 12 (2012) 613–661.

[31] S. Jung, M. K. Tiwari, N. V. Doan, D. Poulikakos, Mechanism of supercooled droplet freezing on surfaces, Nature communications 3 (2012) 1–8.

[32] Y. Hagiwara, S. Ishikawa, R. Kimura, K. Toyohara, Ice growth and interface oscillation of water droplets impinged on a cooling surface, Journal of Crystal Growth 468 (2017) 46–53.

[33] J.-L. Guermond, A. Salgado, A splitting method for incompressible flows with variable density based on a pressure poisson equation, Journal of Computational Physics 228 (2009) 2834–2846.

[34] S. Dong, J. Shen, A time-stepping scheme involving constant coefficient matrices for phase-field simulations of two-phase incompressible flows with large density ratios, Journal of Computational Physics 231 (2012) 5788–5804.

[35] M. S. Dodd, A. Ferrante, A fast pressure-correction method for incompressible two-fluid flows, Journal of Computational Physics 273 (2014) 416–434.

[36] W. J. Boettinger, J. A. Warren, C. Beckermann, A. Karma, Phase-field simulation of solidification, Annual review of materials research 32 (2002) 163–194.

[37] Z. Huang, G. Lin, A. M. Ardekani, Consistent, essentially conservative and balanced-force phase-field method to model incompressible two-phase flows, Journal of Computational Physics 406 (2020) 109192.

[38] J. A. Warren, W. J. Boettinger, Prediction of dendritic growth and microsegregation patterns in a binary alloy using the phase-field method, Acta Metallurgica et Materialia 43 (1995) 689–703.

[39] M. N. Ardekani, L. Al Asmar, F. Picano, L. Brandt, Numerical study of heat transfer in laminar and turbulent pipe flow with finite-size spherical particles, International Journal of Heat and Fluid Flow 71 (2018) 189–199.

[40] C. Beckermann, H.-J. Diepers, I. Steinbach, A. Karma, X. Tong, Modeling melt convection in phase-field simulations of solidification, Journal of Computational Physics 154 (1999) 468–496.

[41] D. Izbassarov, M. E. Rosti, M. N. Ardekani, M. Sarabian, S. Hormozi, L. Brandt, O. Tammisola, Computational modeling of multiphase viscoelastic and elastoviscoplastic flows, International Journal for Numerical Methods in Fluids 88 (2018) 521–543.

[42] A. Shahmardi, S. Zade, M. N. Ardekani, R. J. Poole, F. Lundell, M. E. Rosti, L. Brandt, Turbulent duct flow with polymers, Journal of Fluid Mechanics 859 (2019) 1057–1083.

[43] B. Lalanne, L. R. Villegas, S. Tanguy, F. Risso, On the computation of viscous terms for incompressible two-phase flows with level set/ghost fluid method, Journal of Computational Physics 301 (2015) 289–307.

[44] N. Provatas, K. Elder, Phase-field methods in materials science and engineering, John Wiley & Sons, 2011.

[45] S. Hysing, A new implicit surface tension implementation for interfacial flows, International Journal for Numerical Methods in Fluids 51 (2006) 659–672.

[46] J. Kim, P. Moin, Application of a fractional-step method to incompressible navier-stokes equations, Journal of computational physics 59

(1985) 308–323.

[47] W. B. Hillig, Measurement of interfacial free energy for ice/water system, Journal of crystal growth 183 (1998) 463–468.

[48] A. Carlson, M. Do-Quang, G. Amberg, Modeling of dynamic wetting far from equilibrium, Physics of fluids 21 (2009) 121701.

[49] D. Jacqmin, Contact-line dynamics of a diffuse fluid interface, Journal of Fluid Mechanics 402 (2000) 57–88.

[50] P. Yue, C. Zhou, J. J. Feng, Spontaneous shrinkage of drops and mass conservation in phase-field simulations, Journal of Computational Physics 223 (2007) 1–9.

[51] D. Beaglehole, P. Wilson, Thickness and anisotropy of the ice-water interface, The Journal of Physical Chemistry 97 (1993) 11053–11055.

[52] J. A. Hayward, A. Haymet, The ice/water interface: Molecular dynamics simulations of the basal, prism,{2021}, and {2110} interfaces of ice ih, The Journal of Chemical Physics 114 (2001) 3713–3726.

[53] H. Abels, H. Garcke, G. Grün, Thermodynamically consistent, frame indifferent diffuse interface models for incompressible two-phase flows with different densities, Mathematical Models and Methods in Applied Sciences 22 (2012) 1150013.

[54] X. Xu, Y. Di, H. Yu, Sharp-interface limits of a phase-field model with a generalized navier slip boundary condition for moving contact lines, Journal of Fluid Mechanics 849 (2018) 805–833.